Nanoscale Advances

This article can be cited before page numbers have been issued, to do this please use: M. Hazarika, P. Kumari, C. Saha, L. Lai, H. Singh, M. Huttula and K. Mallick, *Nanoscale Adv.*, 2026, DOI: 10.1039/D6NA00255B.

ROYAL SOCIETY OF CHEMISTRY

rsc.li/nanoscale-advances

View Article Online
DOI: 10.1039/D5NA00255B

Nanosized silver phosphate based asymmetric and symmetric electrochemical capacitors for first and second-order low-pass filter application

Mustafizur R Hazarika[1], Pooja Kumari[1], Chandan Saha[1], Linfei Lai[2], Harishchandra Singh[3, 4], Marko Huttula[3], Kaushik Mallick[1]*

[1] Department of Chemical Sciences, University of Johannesburg, P.O. Box: 524, Auckland Park, 2006, South Africa.
[2] State Key Laboratory of Flexible Electronics, Nanjing Tech University, 30 South Puzhu Road, Nanjing 211816, P. R. China.
[3] Nano and Molecular Systems Research Unit, University of Oulu, FIN-90014, Finland.
[4] Amity Institute of Applied Sciences, Amity University, India, 201313.

* Corresponding author: kaushikm@uj.ac.za (KM)

Abstract:

Nanoscale silver phosphate particles, with a narrow size distribution, were successfully synthesized via a complexation-mediated approach, wherein the growth and dispersion of the particles were effectively controlled by an organic stabilizing matrix. The as-prepared, organically stabilized silver phosphate was employed as an active electrode material in the fabrication of both symmetric and asymmetric electrochemical capacitors. The intrinsic electrochemical properties of the active material (silver phosphate), including redox activity, charge storage performance and kinetic characteristics were systematically determined using three-electrode configuration. The two-electrode systems, both asymmetric and symmetric architecture, were utilized to evaluate the overall performance of the assembled capacitor, including parameters such as cycling stability, specific capacity, energy, power density and energy density. The fabricated asymmetric electrochemical capacitor exhibited a maximum specific capacity of 99 C g^{-1} and delivered an energy density 41 Wh.kg^{-1} with a corresponding power density of 865 W.kg^{-1} at 0.5 A.g^{-1}. The symmetric device attained maximum power and energy density of 2400 W.kg^{-1} and 3.49 Wh.kg^{-1} at 2.4 and 0.6 A.g^{-1}, respectively. The Bode plot displayed the capacitance values of 3.4 and 0.45 mF for the asymmetric and symmetric electrochemical capacitors, respectively. Silver phosphate-based asymmetric and symmetric capacitors were successfully integrated into resistor-capacitor (RC) circuits and systematically evaluated for their performance in both first- and second-order low-pass filter configurations, which enabled a comparative analysis of frequency response characteristics, including attenuation behavior and phase shift.

Keywords: silver phosphate nanoparticles; asymmetric and symmetric devices; power and energy density; resistor-capacitor circuits; first- and second-order filter

1. Introduction:

Rapid consumption of fossil fuel reserves has contributed to rising global temperatures and environmental degradation, prompting an urgent move toward sustainable energy alternatives.[1] Continued reliance on conventional energy systems not only accelerates greenhouse gas emissions but also exacerbates ecological imbalances, further reinforcing the transition toward sustainable and environmentally benign alternatives.[2] Moreover, energy generated through traditional methods is increasingly insufficient to meet the rapidly growing demands of modern society; consequently, considerable efforts are being directed toward developing innovative and efficient strategies for energy generation, storage and utilization to bridge this gap.[3-5] Energy storage devices are critical for stabilizing the variable output of renewable energy sources, ensuring continuous and reliable power delivery, enhancing the overall efficiency and resilience of sustainable energy systems. Conventional energy storage devices primarily include, batteries and capacitors, which store electrical energy through chemical reactions and electrostatic charge accumulation, respectively.[6, 7] Batteries are widely used for their high energy density and long-term storage capabilities, while capacitors offer rapid charge-discharge cycles, making both essential for diverse energy management applications. Supercapacitors, or electrochemical capacitors, represent a hybrid energy storage system positioned between capacitors and batteries. They deliver quick charge-discharge performance along with enhanced energy storage capacity. This unique combination makes them ideal for applications requiring frequent cycling, quick energy delivery and enhanced longevity compared to traditional energy storage devices.[8-10]

Electrochemical capacitors can be broadly classified into two categories; electric double-layer capacitors (EDLC), where charge is accumulated through ion adsorption at the electrode-electrolyte boundary, while pseudocapacitors utilize fast, reversible redox processes to store energy.[11] Carbon-based materials, such as graphene, graphene oxide and carbon nanotubes are commonly employed as electrode materials in EDLC due to their high surface area, excellent chemical, mechanical stability and moderate electrical conductivity.[12-16] Whereas pseudocapacitive materials, like conducting polymers and transition metal compounds, including metal hydroxides, oxides, sulfides, phosphides and phosphates, exhibit significantly higher specific capacitance and enhanced energy storage performance as compared to carbon-based double-layer capacitors, due to their faradaic reactions that enable efficient charge storage at or near the electrode surface.[17-21] It is also important to mention that oxide-based transition metal compounds show special interest as an electrode material for capacitor application owing to their multiple oxidation states, high electrochemical activity, and ability to store charge through fast reversible redox reactions, which provide high specific capacitance and energy density.[22-25]

Among the different kinds of transition metal compounds, silver-based materials have gathered considerable research interest due to their excellent electrochemical properties and promising energy storage performance in applications such as batteries [26, 27] and supercapacitors,[28] due to excellent chemical stability and significant ionic conductivity.[29] An asymmetric device based on silver-cobalt sulfide serving as the cathode in combination with activated carbon as the anode, yielded a specific capacity of 97 $C.g^{-1}$ at a current density of 1 $A.g^{-1}$, along with maximum energy and power densities of 22.34 $Wh.kg^{-1}$ and 899.2 $W.kg^{-1}$, respectively, and exhibited good cycling stability by sustaining 82% of its initial capacity after 1000 consecutive charge-discharge cycles.[30] In a three-electrode system, the working electrode composed of a silver nanoparticle-decorated polypyrrole composite exhibited a specific capacitance of 414 $F.g^{-1}$. This improved electrochemical performance was attributed to the synergistic interaction between the conductive polymer matrix and the electroactive silver nanoparticles. The symmetric device made from the above nanocomposite produced a specific capacitance of 161 $F.g^{-1}$ and exhibited 98.9% of capacitance preservation over 1000 charge-discharge cycles.[31] Niobium silver sulfide ($NbAg_2S$) prepared via a hydrothermal process exhibited a specific capacity of 654 $C.g^{-1}$ in a three-electrode configuration. An asymmetric device made with activated carbon and $NbAg_2S$ produced the specific capacity of 142 $C.g^{-1}$ and provided maximum energy and power density of 43.06 $W.h.kg^{-1}$ and 750 $W.kg^{-1}$, respectively. The device also sustained 93% of initial capacity after 5000 charge-discharge cycles.[32] A silver-polymer hybrid system was applied as the working electrode in a three-electrode setup, where it exhibited a specific capacity of 317 $C.g^{-1}$ at 5 $mV.s^{-1}$ in alkaline electrolyte. The asymmetric device based on an Ag-polymer composite functioning as the cathode and activated carbon as the anode exhibited a specific capacity of 55 $C.g^{-1}$ at a scan rate of 5 $mV.s^{-1}$ and a capacity retention of 85 % after 10^4 charge-discharge cycles at a current density of 1.4 $A.g^{-1}$. The fabricated device also delivered highest energy and power densities of 15.1 $Wh.kg^{-1}$ and 1625 $W.kg^{-1}$, respectively, and demonstrated potential for low-

View Article Online
DOI: 10.1039/D6NA00255B

pass filter applications.[28] It has been reported that silver-nickel oxide, evaluated in a three-electrode configuration, delivered a specific capacity of 824 C. g^{-1} at current density of 2.5 $A.g^{-1}$. The asymmetric device based on silver-nickel oxide as the cathode yielded a specific capacity of 204 $C.g^{-1}$ at 2.5 $A.g^{-1}$, along with the maximum energy and power density of 63.75 $Wh.kg^{-1}$ and 2812.5 $W.kg^{-1}$, respectively.[33] The charge storage performance of mesoporous silver molybdate-based electrode exhibited specific capacity 2610 $C.g^{-1}$ at 1 $A.g^{-1}$ and retained 82 % of capacity after 5000 continuous galvanostatic charge-discharge (GCD) cycles. An asymmetric supercapacitor device, designed silver molybdate and activated carbon as positive and negative electrodes, respectively, yielded maximum specific energy and power of 54 $W.h.kg^{-1}$ and 194 $W.kg^{-1}$, respectively.[34]

This work reports the synthesis of organic molecule-stabilized ultrafine silver phosphate particles via a complexation-mediated route and applied as electrode material in electrochemical capacitor. The incorporation of organic stabilizing agents facilitates controlled nucleation and growth, leading to reduced particle size and improved dispersion, thereby increasing the number of active sites of the material. Reports on silver phosphate-based materials for energy storage systems are very limited;[35, 36] therefore, the goal of this study is to systematically investigate the suitability of organic molecule-stabilized ultrafine silver phosphate as electrode materials for both asymmetric and symmetric electrochemical capacitor applications. We further evaluated the performance of both the asymmetric and symmetric capacitors as low-pass filters in a resistor-capacitor circuit, demonstrating their ability to suppress high-frequency signals while allowing low-frequency components of the input signal to pass. To the best of our knowledge, this work represents the first study to explore nanosized silver phosphate particles for both symmetric and asymmetric supercapacitor configurations and to further demonstrate their applicability in first- and second-order low-pass filter devices.

2. Experimental

2.1 Chemicals:

Silver nitrate, hexamine, disodium hydrogen phosphate, carbon black, potassium hydroxide (KOH), N-methyl pyrrolidone (NMP), and PVDF used in this study were procured from Sigma-Aldrich, and activated carbon (AC) was obtained from the Fuel Cell Store.

2.2. Synthesis of silver phosphate (SPO) nanoparticles: To synthesize silver phosphate (SPO), 1.5 mg of hexamethylenetetramine (hexamine) was dissolved in methanol (10 mL). In the methanolic solution, 5 mL of an aqueous $AgNO_3$ solution (10^{-2} M) was slowly added, leading to the formation of a white precipitate of Ag(I)-hexamine complex. Subsequently, 5 mL of Na_2HPO_4 (10^{-1} M) solution was introduced dropwise into the earlier formed precipitate with constant stirring. A light-yellow solid mass was obtained, which is indicative of the formation of silver phosphate, consistent with its characteristic coloration. The above-mentioned synthesis protocol was performed under ambient pressure and temperature condition. The resulting product was collected via filtration and characterized using various analytical techniques to confirm the structural, morphological, and compositional properties. The ass synthesized silver phosphate was also employed as the active material in electrochemical capacitor applications to evaluate its energy storage and electronics performance.

2.3. Electrode fabrication:

2.3.1. Working electrode preparation for three electrode system: The three-electrode setup comprises of a Ni-foam as working electrode, a calomel ($Hg\text{-}Hg_2Cl_2$) as reference electrode and a Pt-wire as counter electrode. To construct the working electrode, a homogeneous slurry, containing conductive carbon, polyvinylidene fluoride (PVDF) and SPO, was prepared in N-methyl-2-pyrrolidone (NMP) using 1:1:8 as mass ratio. The resulting mixture was uniformly applied on a nickel foam substrate (1×1 cm^2). The coated electrode was vacuum dried at 70 °C and later utilized for electrochemical characterization.

2.3.2. Fabrication of asymmetric electrochemical capacitor: An asymmetric device was configured using SPO as the (cathodic) electrode and activated carbon (AC) as the (anodic) electrode. The fabrication of the cathode was carried out following the procedure outlined in section 2.3.1. The anode was formed by preparing a slurry of activated carbon (AC) and PVDF (95:5 by mass) in NMP, which was then coated onto nickel foam (1×1 cm^2) and dried under vacuum at 70 °C. A filter paper soaked in KOH electrolyte (2 M) was used as the separator and placed between the two electrodes during coin cell (CR2032) assembly. Using the mass balance equation, $m^-/m^+ = (Cs^+ \times \Delta V^+)/(Cs^- \times \Delta V^-)$, the mass ratio between the negative and positive electrodes was calculated 4.2. The Cs^+ and Cs^- represent the specific capacities of the positive and negative electrodes, respectively, obtained from the GCD curves measured in the three-electrode configuration. The notations ΔV^+ and ΔV^- denote the potential windows of the positive and negative electrodes, while m^+ and m^- correspond to the masses of the active electrode materials. The total active mass loading ($m^+ + m^-$) for the assembled device was 5.2 mg.

2.3.3. Fabrication of symmetric electrochemical capacitor: For the construction of the symmetric device, two identical pieces of Ni-foam electrodes coated with SPO were used, and KOH (2M) functioned as the electrolyte. The mass loading calculation for the device was done by using the equation used in section 2.3.2. An optimal mass ratio of $m^{-}/m^{+} = 1$ was optimized to construct the symmetric device. The total active material loading $(m^{+} + m^{-})$ for the assembled device was 3.0 mg. The Biologic SP-300 potentiostat was used to investigate the electrochemical performance of both the devices.

3. Results and Discussion:

The synthesis of hexamine-stabilized silver phosphate nanoparticles was achieved through two-step complexation-mediated process. In the initial step, controlled complex formation between the silver precursor and hexamine facilitated the development of nucleation centres. The complexation arises from the coordination interaction between electron-rich nitrogen atoms of hexamine and silver cation, leading to the formation of an Ag(I)-hexamine complex. In the subsequent step, the addition of disodium hydrogen phosphate induced the reaction between silver (I) and phosphate anion promoting the formation of uniformly distributed and well-defined hexamine stabilized silver phosphate (Ag_3PO_4) nanoparticles.

X-ray diffraction (XRD) was employed to analyze the crystal structure of the prepared silver phosphate over a 2θ range of 20-90°, figure 1A. The diffraction pattern displayed prominent peaks at 20.75°, 29.51°, 33.09°, 36.35°, 42.23°, 47.50°, 52.36°, 54.67°, 56.92°, 61.25°, 71.41°, and 86.60°, corresponding to the (110), (200), (210), (211), (220), (310), (222), (320), (321), (400), (421) and (520) planes.[37] The diffraction peaks are in excellent agreement with standard data ICDD: 04-010-1988, which confirms the formation of a pure cubic phase with space group of P-43n.[38] The lattice parameters were determined to be a = b = c = 6.048 Å and lattice angle α = b = γ = 90°. According to the unit cell structure, (figure1A, inset), each Ag atom is bonded to four equivalent O in a distorted square-planar geometry with Ag-O bond lengths of 2.37 Å, while P is tetrahedrally coordinated to four oxygen atoms forming P-O bonds with the bond lengths of 1.55 Å. Each O is connected to one P and three Ag atom, forming distorted corner-sharing OAg_3P tetrahedra. According to the unit-cell structure, both silver and phosphorus atoms exhibit coordination with four oxygen atoms, generating interconnected AgO_4 and PO_4 tetrahedral clusters.[39] Each isolated PO_4 unit bonds to three adjacent AgO_4 units through shared oxygen atoms, creating a robust three-dimensional network. This arrangement contributes to the high stability and symmetry of the cubic Ag_3PO_4 framework. X-ray photoelectron spectroscopy (XPS) was employed to investigate the

View Article Online
DOI: 10.1039/D6NA00255B

chemical states and the composition of hexamine-stabilized silver phosphate. The survey spectrum, figure 1B, confirms the presence of Ag 3d, P 2p, O 1s, C 1s, and N 1s peaks, indicating the successful integration of silver, phosphorus, oxygen and hexamine-derived elements, carbon and nitrogen, within the material. The high-resolution Ag 3d spectrum, (figure 1B, inset), exhibits a well-defined doublet arising from spin-orbit splitting, with characteristic peaks located at binding energies of 367.9 and 373.7 eV, corresponding to the Ag $3d_{5/2}$ and Ag $3d_{3/2}$ orbitals, respectively. The observed energy separation and peak positions are in good agreement with reported values for Ag (I) species, confirming that silver is in the +1-oxidation state within hexamine-stabilized silver phosphate structure.[36] The deconvoluted high resolution P2p spectrum, figure 1C, revealed peaks at 132.4 eV and 133.8 eV, corresponding to $2p_{3/2}$ and $2p_{1/2}$ spin orbits, respectively, suggesting the presence of PO_4^{3-} (phosphate) chemical environment.[40, 41] Similarly, deconvoluted O1s spectrum, figure 1D, displayed two peaks at 530.8 and 532.4 eV, which are attributed to lattice oxygen (O^{2-}) and surface hydroxyl groups, respectively.[41] The high-resolution C1s core-level spectrum can be deconvoluted into two peaks with binding energies at 284.6 and 285.7, which corresponds to C-H and C-N species, respectively, figure 1E.[42] The N 1s XPS spectrum, figure 1F displays a single broad peak corresponding to nitrogen species at 399.35 eV, attributed to N-C bonds.[43]

Figure 2, displays the TEM (transmission electron microscopy) images of the synthesized silver phosphate nanoparticles acquired at different magnifications, providing detailed insight into their morphological characteristics. As shown in figure 2 (A and B), the dark-field TEM images display that the nanoparticles, with sizes ranging from approximately 4-8 nm, are uniformly dispersed across the organic matrix, indicating effective stabilization and prevention of agglomeration. The distinct bright contrast observed in these images corresponds to the silver phosphate nanoparticles, arising from their higher electron scattering ability compared to the surrounding organic matrix. Figure 2C displays a high-resolution TEM image of single nanoparticle, clearly revealing well-defined lattice fringes, indicates high degree of crystallinity of the particle. The SEM image, figure 3A, reveals a densely packed, three-dimensional nanostructured morphology corresponding to a hexamine-stabilized silver phosphate organic-inorganic hybrid composite. The composite surface appears highly rough and porous, with irregular, architectures formed through the assembly and intergrowth of smaller building units. Such a morphology is indicative of effective interaction between the organic (hexamine) matrix and inorganic silver phosphate phase, contributing to structural stability while providing many accessible active sites. The elemental mapping analysis provides further evidence about the homogeneous distribution of

View Article Online
DOI: 10.1039/D6NA00255B

the constituent elements, silver, phosphorus, and oxygen (originating from silver phosphate), along with nitrogen and carbon (derived from hexamine), as validated by energy-dispersive X-ray spectroscopy (EDX) analysis, figure 3B. The absence of any extra elemental signals in the EDX spectrum confirms the high-level purity of the material and suggests that no detectable impurities are present within the detection limits of the technique. The elemental maps clearly demonstrate that all five elements, Ag, P, O, N and C are uniformly and homogeneously distributed throughout the hexamine-stabilized silver phosphate hybrid composite, figure 3 (C-G), with the average weight % (surface) of 52.85, 10.6, 15.56, 10.88 and 10.11%, respectively.

Silver phosphate exhibits a total of 18 Raman-active vibrational modes according to theoretical predictions. However, only a few of these modes are clearly resolved in the experimental Raman spectrum, figure 4A. The observed bands are primarily assigned to the internal vibrational modes of the phosphate [PO_4^{3-}] tetrahedral units, including both stretching (symmetric and asymmetric) and bending modes. The remaining Raman-active modes are either weak or overlapped and therefore are not distinctly identified in the spectrum. The vibrational bands located at 913 and 1008 cm^{-1} correspond to symmetric and asymmetric stretching of O-P-O bonds, respectively, while the signal at 558 cm^{-1} is due to asymmetric bending modes of PO_4^{3-} clusters. The absorptions at 102 and 221 cm^{-1} are attributed to rotational and translational motions of the clusters.[44-47] These low-frequency modes correspond to external lattice vibrations, arising from the collective movement of the phosphate units within the crystal framework. An unassigned broad peak observed around 710 cm^{-1} may be attributed to the C-N network vibrations originating from the hexamine molecule. This broad feature likely arises from coupled C–N stretching and skeletal deformation modes associated with amine framework, indicating the presence of coordinated hexamine species within the synthesized material.[48] In the FTIR spectrum of hexamine stabilized silver phosphate, a prominent asymmetric absorption band was observed in the phosphate stretching region. The peak centered at 954 cm^{-1} is attributed to the symmetric stretching vibration of P-O of the phosphate group. At a slightly higher wavenumber, around 1006 cm^{-1}, a shoulder-like feature appears, which corresponds to the asymmetric stretching vibration of the P-O bond. The presence of this shoulder indicates slight distortion or reduced symmetry within the phosphate tetrahedral environment, possibly arising from coordination effects with the lattice. The P-O-P bending vibrations are observed at 547 cm^{-1}, characteristic of bridging oxygen atoms linking adjacent phosphate units and confirms the connectivity of the phosphate tetrahedra.[46] The vibrational modes observed at 1460, 1370, 1325, 1231, 806,

View Article Online
DOI: 10.1039/D6NA00255B

680 and 505 cm^{-1} are associated with the methylene (-CH_2-) groups of hexamine.[49] The bands in the higher wavenumber region are mainly attributed to bending and deformation vibrations of the -CH_2-units, while those appearing at lower wavenumbers correspond to rocking, scissoring and wagging motions coupled with the C-N framework.

3.1. Electrochemical properties of the capacitor:

Three electrode system: The electrochemical performance of silver phosphate (SPO)-modified nickel foam as the working electrode was examined through cyclic voltammetry (CV) technique. Figure 5A illustrates the voltammograms of the electrode obtained in KOH (2M) electrolyte at a scan rate of 4-50 mV.s^{-1} over a potential range from -0.1 to 0.6 V. The CV curves exhibit distinct redox peaks, characteristic of pseudocapacitive behaviour.[50] Two anodic peaks are observed in the potential ranges of 0.35-0.40 V and 0.54-0.56 V, while a broad cathodic peak with an overlapping feature, suggesting the occurrence of multiple redox processes. The redox chemistry of Ag (I) in silver phosphate can be significantly influenced by the incorporation of nitrogen-containing ligands. Coordination of N-donor ligands alters the local electronic environment of Ag^+ centres and facilitates electron transfer processes within the framework. Under such conditions, the Ag (I) species may undergo a disproportionation reaction in presence of electrolyte, leading to the formation of a mixed oxidation state composed of Ag (II) and metallic Ag (0).[51] The Ag (II) ion is more likely to be coordinated with four donor nitrogen atoms of the hexamine ligand, forming a square-planar coordination geometry. This arrangement arises from the strong interaction between the nitrogen atoms and the Ag (II) centre, which stabilizes the higher oxidation state of silver.[51] During the electrochemical reaction, two anodic peaks appeared at the above-mentioned potential ranges correspond to Ag (0) to Ag (I) and Ag (I) to Ag (II). The specific capacity of the electrode was measured to be 281 C.g^{-1} at 4 mV.s^{-1}, indicating efficient charge storage at lower scan rates. As the scan rate increased to 50 mV.s^{-1}, the specific capacity decreased to 116 C.g^{-1}. The decrease in specific capacity at higher scan rates is primarily attributed to restricted ion diffusion, which limits the time available for complete redox reactions and consequently reduces the utilization of the active material. The specific capacity (Cs) expressed in $C.g^{-1}$ was calculated using the equation $Cs = \int IdV/(\vartheta \times m)$, where IdV represent integrated area under the CV curve, ϑ is scan rate and m corresponds to the mass of active material (g). Figure 5B presents the galvanostatic charge-discharge (GCD) profiles of the SPO-modified electrode recorded at current densities ranging from 1.0 to 5.8 A.g^{-1} within the potential range of -0.1 V - 0.6 V. The observed non-linearity in the GCD profiles points to faradaic redox reactions as the primary mechanism of energy storage[52] rather than double-layer capacitance.[53] The observed behaviour demonstrates that the electrode material participates in electrochemical reactions, leading to enhanced charge storage performance. The discharge curves exhibit a kink pattern, attributed to the oxidation of residual metallic silver present in the electrode material.[52, 54, 55] The pronounced IR drop observed in the GCD curves is attributed to the intrinsic resistance of the electrode, charge-transfer resistance, and restricted ion diffusion within the electrode structure.[56] Based on the obtained GCD profiles, the specific capacity (C_S) values in C.g^{-1} can be determined using the equation, $C_S = I \times \Delta t / m$, where, I represent current (A), m is the mass of the active material and t correspond with time.

Figure 5C displays the specific capacity values obtained for the SPO-modified electrode under different current densities. At a current density of 1.0 A.g^{-1}, the electrode exhibits a specific capacity of 211 C.g^{-1}. However, as the current density increases, the capacity decreases noticeably, reaching 85 C.g^{-1} at 5.8 A g^{-1}. This decline can be ascribed to the limited diffusion of electrolyte ions and the reduced accessibility of active sites at higher current densities, which restricts complete utilization of the electroactive material.[57-59] The calculated specific capacity values were 211, 175, 150, 132, 117, 106, 98, 91 and 85 C.g^{-1} at applied current densities of 1.0, 1.6, 2.2, 2.8, 3.4, 4.0, 4.6, 5.2 and 5.8 A.g^{-1}, respectively. The moderately high-capacity values can be attributed to the structural design of the electrode, which promotes enhanced electrolyte ion accessibility, efficient ion diffusion and rapid electron transport. However, the gradual decrease in specific capacity with increasing current density can be attributed to limited ion diffusion, incomplete utilization of electroactive sites, enhanced polarization, and mass-transport constraints, which collectively restrict the electrochemical participation of the active material. Both CV and GCD analyses confirmed pseudocapacitive electrochemical behaviour of the electrode. The long-term electrochemical stability of the electrode was assessed through 2000 consecutive charge-discharge cycles at current density of 2.2 A.g^{-1} to evaluate its durability and capacity retention during repeated electrochemical operation. The electrode demonstrated excellent stability, sustaining 91 % of its initial capacity and maintaining a Coulombic efficiency of 99 % after 2000 cycles, 5D, upper panel. Figure 5D, lower panel shows the first- and last-five charge-discharge curves, revealing minimal changes in shape, further confirming the good cyclic stability of the electrode.

View Article Online
DOI: 10.1039/D6NA00255B

Electrochemical impedance spectroscopy (EIS) measurements were carried out within the frequency range from 100 mHz to 200 kHz, and the resulting impedance response was analyzed using Nyquist plot and subsequently modelled using an equivalent electrical circuit, figure S1 (A), supporting information. The frequency window enables the investigation of different electrochemical processes, including electrolyte resistance, charge transfer at the interface of the electrode-electrolyte and diffusion of the ion within the electrode material. The circuit consists of the solution resistance (R_S), double-layer capacitance (C_{dl}), charge transfer resistance (R_{ct}), occurring at the electrode-electrolyte interface, constant phase element (Q_2), non-ideal capacitive component and Warburg impedance (W). In the circuit, R_S is connected in series with the rest of the circuit elements. The remaining circuit consists of a parallel network composed of Q_2 and R_{ct} connected in series with C_{dl}. Finally, the circuit includes the Warburg impedance in series, which represents the diffusion-controlled transport of electrolyte ions within the electrode material and electrolyte. From the fitting results, the R_S and R_{ct} values were determined to be 1.65 Ω and 2.26 Ω, respectively.

3.2. SPO-based asymmetric electrochemical capacitor: Figure S1 (B), supporting information, shows the comparative CV curves of SPO (from -0.1 to 0.6 V) and AC (from -0.8 to 0.0 V). Figure 6A portrays the electrochemical performance of the assembled asymmetric device within a potential window of 1.5 V, where ΔV (device) = ΔV positive (0.7 V) + ΔV negative (0.8 V), recorded at scan rates ranging from 4 to 50 $mV.s^{-1}$. The device achieved a maximum specific capacity (20.14 $C.g^{-1}$) at 4 $mV.s^{-1}$ which decreased to 7.72 $C.g^{-1}$ at 50 $mV.s^{-1}$. The CV curves exhibited nonlinear profiles, revealing the coexistence of electric double-layer capacitance (EDLC) and Faradic processes, which confirms the pseudocapacitive behaviour of the device.[60] The CV profiles maintain their characteristic shape even at elevated scan rates, reflecting the good rate performance and stability of the device.[61] The GCD study was conducted to analyze the actual charge-discharge duration of the device and to evaluate electrochemical performance, particularly charge storage and rate capability, and reversibility under constant current conditions. This technique enables the estimation of electrochemical parameters such as coulombic efficiency, specific capacity and performance indicators like energy and power density.[62] In this study, the GCD profiles of the cell were measured at current densities ranging from 0.5 to 1.7 $A.g^{-1}$, figure 6B. The specific capacity reached a value of 99 $C.g^{-1}$ at a current density of 0.5 $A.g^{-1}$, which gradually decreased to 85 $C.g^{-1}$ at 1.7 $A.g^{-1}$, reflecting the typical reduction in capacity at higher current densities due to limited ion diffusion and reduced utilization of electroactive sites within the

View Article Online
DOI: 10.1039/D6NA00255B

electrode material. The non-triangular characteristics of the GCD curves, confirm that the electrochemical behaviour is predominantly governed by Faradaic redox reactions. To assess long-term cycling behaviour of the capacitor, the device was tested under 5000 continuous charge-discharge cycles at a current density of 0.9 A.g^{-1}. The device sustained 86 % of its initial capacity at the end of the cycling process and maintained a Coulombic efficiency of 94 %, figure 6C, upper panel. The nearly identical GCD profiles, figure 6C, lower panel, of the initial and final five cycles confirm the structural robustness and long-term electrochemical stability of the device, indicating that the electrode materials maintain their integrity and electrochemical activity throughout repeated charge-discharge processes.[63] The device reached a maximum power density (P) of 2596 W.kg^{-1} at an energy density (E) of 35.59 Wh.kg^{-1}. Furthermore, the asymmetric device delivered an energy density of 41 Wh.kg^{-1} with a corresponding power density of 865 W.kg^{-1} at a current density of 0.5 A.g^{-1}, highlighting its promising energy storage capability and efficient power delivery for electrochemical energy storage applications, figure 6D. The energy and power density were calculated using the equations: $E\ (Wh.kg^{-1}) = C_S \Delta V/(2\times 3.6)$ and $P\ (W.kg^{-1}) = (E\times 3600)/\Delta t$.[64, 65] The electrochemical performance of various silver-based electrode materials used in supercapacitor applications is presented in the supporting information, table S1, for ready reference.

By applying the power law relationship between current and scan rate, the charge storage behaviour of the device was evaluated to elucidate whether surface-controlled capacitive processes or diffusion-limited Faradaic reactions are predominant.[66] According to power law, the corelation between scan rate and peak current can be represented as $I = a\vartheta^b$ (I represent peak current, a is a constant, ϑ denotes scan rate and b indicating the charge storage mechanism) and by applying the logarithm of both sides of the equation, the relationship can be rewritten in a linear form as: $\log(I) = \log\ (a) + b\ log\ (\vartheta)$.[67] Ideal capacitive behaviour is indicated by b = 1, while b = 0.5 corresponds to a diffusion-limited, battery-type storage process.[67, 68] As illustrated in figure 7A for the present asymmetric device, the b-value was found to be 0.66 and 0.71 for anodic and cathodic peaks, respectively, confirming a diffusion-controlled dominated mechanism. The capacitive and diffusion contributions was separated using the relation $I = I_{cap} + I_{diff} = k_1 v + k_2 v^{1/2}$ ($k_1 v$ denotes surface capacitive contribution and $k_2 v^{1/2}$ represents diffusion-controlled contribution), which can be represented as $I/\sqrt{v} = k_1\sqrt{v} + k_2$.[69] By plotting $I/\sqrt{v}$ vs. $\sqrt{v}$, the slope and intercept provide the values of k_1 and k_2, respectively. Based on the experimental CV curves, figure

6A, recorded at scan rates ranging from 4 to 50 mV.s^{-1}, the asymmetric device exhibited a capacitive contribution of 30.37 % at a scan rate of 4 mV.s^{-1}. As the scan rate increased, the capacitive contribution progressively increased, reaching 60.66 % at 50 mV.s^{-1}, figure 7B. The increase in capacitive contribution with increasing scan rate suggests that the charge storage process becomes progressively dominated by surface-controlled mechanisms. At higher scan rates, the limited time available for electrolyte ions to diffuse into the bulk of the active material suppresses diffusion-controlled (faradaic) processes, thereby enhancing the contribution from rapid surface redox reactions (pseudocapacitance) and electrostatic charge accumulation at the electrode-electrolyte interface (electric double-layer capacitance).[70] Figure S1 (C), supporting information, illustrates the Nyquist plot of the device, accompanied by the corresponding equivalent circuit model in the inset, measured over a frequency range of 100 mHz to 200 kHz. Analysis of the impedance data reveals a solution resistance (R_S) of 2.386 Ω, representing the inherent resistance of the electrolyte and electrode contacts, and a charge transfer resistance (R_{ct}) of 4.707 Ω, indicating the resistance associated with the electrochemical reactions at the electrode-electrolyte interface. Figure 7C presents the Bode plots of the device, illustrating the variation of phase angle with frequency, where at low frequencies the phase angles reach -77.78°, confirming capacitive behaviour. Figure 7D, illustrate the variation of imaginary capacitance, $C''(\omega)$, and real capacitance, $C'(\omega)$, components of the electrochemical capacitor with frequency (f) and derived using the relations $Z'(\omega) = 2\pi f C''(\omega)|Z(\omega)|$ and $Z''(\omega) = 2\pi f C'(\omega)|Z(\omega)|$, where $\omega = 2\pi f$ denotes the angular frequency and Z represents impedance.[71, 72] The real capacitance is the capacitance (F) of the device which is usable with the value of 3.4 mF. The C'' versus frequency plot showed a peak at 3.35 Hz, corresponding to a relaxation time (τ) of 0.29 s, suggests a fast charge-discharge response of the device.

3.3. SPO-based symmetric electrochemical capacitor: Figure 8A displays the CV profiles of the SPO-based symmetric device, demonstrating stable electrochemical behaviour within the potential window range of 0.0-0.9 V. The measurements were recorded at scan rates ranging from 10 to 70 mV s^{-1} in the presence of 2 M KOH electrolyte. The device achieved a maximum specific capacity of 8.66 C.g^{-1} at 10 mV.s^{-1} which decreased to 1.64 C.g^{-1} at 70 mV.s^{-1}. A quasi-rectangular CV profile indicates the pseudocapacitive behaviour of the device.[73] With increasing scan rate a proportional and symmetrical enhancement in current response, suggesting effective electron transport within the conductive pathways of the device.[74] The GCD profiles, figure 8B, of the of the cell were recorded at current densities ranging from (0.6 - 2.4 A.g^{-1}). The non-triangular charge-discharge curves imply that the storage mechanism is dominated by reversible electrochemical redox process.[75] The specific capacity reached a value of 21.41 C.g^{-1} at 0.6 A.g^{-1} which gradually decreased to 7.01 C.g^{-1} at 2.4 A.g^{-1}. The device was tested under 5000 continuous GCD-cycles at a current density of 1.2 A.g^{-1} and achieved 87% capacity retention with 93% coulombic efficiency after 5000 cycles, figure 8C, upper panel, demonstrating good stability. The close similarity between the initial and final GCD curves demonstrates the excellent structural integrity and long-term electrochemical stability of the electrode material, figure 8C, lower panel. The correlation between power and energy density as a function of current density is presented in figure 8D. The device attained maximum power and energy density of 2400 W.kg^{-1} and 3.49 Wh.kg^{-1} at 2.4 and 0.6 A.g^{-1}, respectively. As illustrated in 9A, for the symmetric device, the b-values were found to be 0.60 (anodic) and 0.76 (cathodic) peaks respectively, confirming a diffusion-controlled dominated mechanism. The bar chart, figure 9B, clearly shows the progressive increase in capacitive contribution with increasing scan rate. The SPO based symmetric device exhibited a capacitive contribution of 32.48 % at 10 mV. s^{-1}, which increased to 57.63 % at 70 mV. s^{-1}. Electrochemical impedance spectroscopy of the SPO-based symmetric device was performed within the frequency range of 100 mHz-200 kHz to investigate the charge transfer and ion transport behaviour, figure S1 (D). The equivalent circuit analysis, figure S1 (D), inset, of the symmetric device revealed solution resistance (R_S) of 2.632 Ω and charge transfer resistance (R_{ct}) of 13.24 Ω. The Bode plot of the symmetric device is presented in Figure 9C, illustrating the relation between phase angle and frequency. At low frequencies, the phase angles reach -82.28° for the symmetric device which confirms capacitive behaviour of the device. The symmetric device displayed usable capacitance of 0.45 mF with a peak frequency of 20.83 Hz, yielding a relaxation time (τ) of 0.048 s, figure 9D.

The Bode plot analysis displayed capacitance values of 3.4 mF and 0.45 mF for the asymmetric and symmetric devices, respectively. The notable difference in capacitance values, for the asymmetric and symmetric devices, indicates the superior charge storage capability of the asymmetric configuration, which can be ascribed to the synergistic interaction between the dissimilar electrode materials and an extended operating potential window. In contrast, the relatively lower capacitance of the symmetric device reflects its limited electrochemical performance arising from identical electrode composition.

3.4. First and second order low pass filter: Passive RC, resistors (R) and capacitors (C), filters remove unwanted signals by selectively allowing only sinusoidal input signals of certain frequencies to pass through. The low pass filter (LPF) allows signals with frequencies up to its cut-off frequency (f_c) to pass through, while attenuating signals with frequencies higher than f_c. In this work, silver phosphate based asymmetric (C_1) and symmetric (C_2) capacitors with the capacitance values of 3.4 and 0.45 mF, extracted from figure 7D and 9D, respectively, are considered for the filter application. The performance of the filters was evaluated using MATLAB simulations and validated through hardware implementation. The first order LPF was built by connecting one resistor (R) and one capacitor (C) in series with applied sinusoidal input signal (V_{in}) while the output (V_{out}) was measured across the capacitor, figure 10 (A and B).[76] The second order LPF was constructed by cascading the two passive first order low pass filters used as above, figure 10 (C and D).[77] The load and output impedance are determined by the resistor, whereas the capacitor provides frequency-dependent impedance for filtering purposes. At the cut-off frequency, the V_{out} dropped by $\approx$ 70.5% and 70.8 % with corresponding to the maximum applied input signal ((V_{in} = 1.6 V peak-peak), figure 11 (A and B). In this study, we analysed the performance of first order LPF circuits using R_1 = 50 kΩ and C_1 = 3.4 mF for the asymmetric configuration, and R_2 = 500 kΩ and C_2 = 0.45 mF (from EIS) for the symmetric configuration, figure 11 (A and B). The time constants, ($\tau = \mathrm{R} \times \mathrm{C}$), are ~ 170 ($\tau_1$) and ~ 225 ($\tau_2$) sec for the asymmetric and symmetric first order low pass filter setup, respectively. The cut-off frequency or -3 dB point corresponding to $f_c = 1/2\pi RC$, for asymmetric and symmetric capacitor-based first order LPFs, yielded f_c = 0.93 mHz and 0.7 mHz respectively.[73] Bode plot analysis, at cut-off frequency, shows voltage gains of -3 dB with – 44.96° phase lag for the asymmetric (asym) and -3.01 dB with – 44.9° phase lag for the symmetric (sym) configuration, figure 12 (A and B), respectively. Figure 12A exhibits magnitude response that decreases at rate of -19.96 dB/decade, and -19.97 dB /decade roll off after the cut off frequency in the asymmetric and symmetric based filters, respectively. The effective time constant of the second order RC-cascaded low pass filter circuit is approximated using $\tau = (R_1C_1R_2C_2)^{1/2} = 195$ sec.[78] The cut off frequency was calculated using the equation $(1+\omega^2\tau_1^2)(1+\omega^2\tau_2^2) = 2$ was found to be 0.51 mHz, figure 11C, at -3.01 dB with a phase lag of – 65.1°, figure 12 (A and B).[79] The damping factor calculated using the expression, $\zeta = B/2\sqrt{A}$, where $A = R_1R_2C_1C_1$ and $B = R_1C_1 + R_2C_2 + R_1C_2$ was found to be $\approx$ 0.9, an underdamped second-order filter. From the magnitude response of Bode plot, the slope roll-off after cut-off frequency was observed to be $-39.8\ dB/decade$, figure 12A. The experimental findings of the low pass filters are in close agreement with the theoretical predictions, demonstrating consistency within the expected limits. The fabricated capacitors have been successfully implemented in low pass filter circuits which can be used effectively to attenuate high-frequency noise. It is important to mention that ultra-low sub-Hertz cut-offs frequency in the range between 0.1 Hz and 0.001 Hz can be used in filter applications for physiological signal conditioning.[80]

4. Conclusion:

In this work, hexamine-stabilized silver phosphate nanoparticles were successfully obtained using a two-stage complexation-mediated synthesis route. In the initial step, controlled complex formation between the silver precursor and hexamine, while the subsequent step with the addition of disodium hydrogen phosphate promoted the formation of uniformly distributed silver phosphate nanoparticles. The organic molecule-stabilized silver phosphate was implemented as an active material for the fabrication of electrochemical capacitors in both asymmetric and symmetric configurations. The capacitive behavior of the fabricated devices was systematically evaluated using Bode plot analysis, where the asymmetric configuration exhibited a usable capacitance value of 3.4 mF, significantly higher than the 0.45 mF observed for the symmetric device. This difference highlights the improved electrochemical storage performance of the asymmetric system, which can be ascribed to the complementary potential windows and synergistic interaction between the dissimilar electrode materials. In contrast, the symmetric device, composed of identical electrodes, showed comparatively lower capacitance due to its limited operating voltage range and less efficient utilization of active material. The successful integration of asymmetric and symmetric electrochemical capacitors into RC circuits for first- and second-order low-pass filter applications demonstrated their practical versatility beyond conventional energy storage. These devices effectively combine charge storage capability with frequency-selective behavior, enabling controlled signal attenuation and phase response.

View Article Online
DOI: 10.1039/D6NA00255B

Authorship contribution

MRH: conceptualization, experimental work, data curation, simulation and draft writing; PK: experimental work and material characterization; CS: material characterization; LL: material characterization; HS: XPS analysis; MH: material characterization; KM: conceptualization, supervising, funding, review and editing.

Conflicts of interest

The authors declare no conflict of interest.

Acknowledgements

This study was financially supported by the Faculty of Science and University Research Council, University of Johannesburg. HS and MH acknowledge the support from the Strategic Research Council within the Research Council of Finland decision 358422 and JustH2Transit and Profi7/H2FUTURE (352788). HS also acknowledges the financial support from the ANRF, Department of Science and Technology, India, through the Ramanujan Faculty Award (RJF/2023/000058).

Data availability

The data that support the findings of this study are available from the corresponding author, upon reasonable request.

View Article Online
DOI: 10.1039/D6NA00255B

References:

1 M. Armand and J.M. Tarascon, *Nature,* 451, 2008, 652-657.

2 D. Larcher and J.M. Tarascon, *Nat. Chem.* 7, 2015, 19-29.

3 Y. Zhang, J. Wei, Y. Zhu and G. George-Ufot, *J. Clean. Prod.*, 263, 2020, 121584.

4 J. P. Sidhu, W. Ahmed, W. Gernjak, R. Aryal, D. McCarthy, A. Palmer, P. Kolotelo and S. Toze, *Sci. Total Environ.*, 463, 2013, 488-496.

5 S. S. Akadiri, A. A. Alola, G. O.Williams and M. U. Etokakpan, *Sci. Total Environ.*, 708, 2020, 134653.

6 E. Kurian, J. Pitchai, D. Kumar, S. Jose and K. Ramesha, *Batteries & Supercaps*, 9, 2026, e202500435.

7 L.M. Liu, J. L. Qu, A. J. Gu and B. H. Wang, *J. Mater. Chem. A*, 8, 2020, 18515–18537.

8 L. L. Zhang and X. Zhao, *Chem. Soc. Rev.,* 38, 2009, 2520-2531.

9 Q. Lu, M. W. Lattanzi, Y. Chen, X. Kou, W. Li, X. Fan, K. M. Unruh, J. G. Chen and J. Q. Xiao, *Angew. Chem. Int. Ed.,* 50, 2011, 6847-6850.

10 S. Haque, J. Ferraris, K. Balkus, *Batteries & Supercaps*, 9, 2026, e202500894.

11 B.E. Conway and W.G. Pell, *J. Solid State Electrochem.,* 7, 2003, 637–644.

12 E. Frackowiak, *Phys. Chem. Chem. Phys*., 9, 2007, 1774-1785.

13 A. Velasco, Y. Ryu, A Bosca, A. Ladron-de-Guevara, E. Hunt, J. Zuo, J. Pedros, F. Calle and J. Martinez, *Sustain. Energy Fuels*, 5, 2021, 1235–1254.

14 M. Down, S. R. Neale, G. C. Smith, and C. E. Banks, *ACS Appl. Energy Mater*., 1, 2018, 707-714.

15 L. Yang, L. Zhang, X. Jiao, Y. Qiu and W. Xu, *RSC Adv*., 11, 2021, 4042-4052.

16 C. Cao, Y. Zhou, S. Ubnoske, J. Zang, Y. Cao, P. Henry, C. Parker and J. Glass, *Adv Energy Mater.,* 9, 2019, 1900611-1900618.

17 G. Snook, P. Kao and A. Best, *J. Power Sources*, 196, 2011, 1-12.

18 S. Mali, D. Late, B. Sathe, *Fundamentals and supercapacitor applications of 2D materials*, Elsevier, 2021.

19 C. An, Y. Zhang, H. Guo and Y. Wang, *Nanoscale Adv.,* 1, 2019, 4644-4658.

20 M. Zhu, D. Wang, Z. Ge, L. Pan, Y. Chen, W. Wang, N. Mitsuzaki, S. Jia and Z. Chen, *Chem. Commun*., 61, 2025, 8314-8326**.**

21 X. Li, A. Elshahawy, C. Guan and J. Wang, *Small*, 13, 2017, 1701530.

22 X. Zhang, Y. Wei, X. Yang, C. Hou, Y. Chen and D. Wang, *J. Energy Storage,* 2025, 122, 116677.

23 J. Zhang, Y. Wei, X. Yang, D. Wang, C. Hou and Y. Chen, *J. Alloys Compd.,* 2025, 1032, 181141.

24 L. Chen, X. Zhang, Z. Wang, X. Kong, J. Zhang, J. Zeng and D. Wang, *Chem. Eng. J.,* 2024, 500, 157472.

25 X. Han, J. Zhang, Z. Wang, H. Younus and D. Wang, *Rare Met.,* 2024, 43, 5734-5746

26 M. Bhute, S. Mitra and S. Kondawar, *Mater. Lett.,* 236, 2019, 225-228.

27 A. Karpinski, S. Russell, J. Serenyi and J. Murphy, *J. Power Sources*, 91, 2000, 77–82.

28 P. Kumari, C. Saha, S. Ghosh, V. Perla, H. Singh and K. Mallick, New J. Chem., 49, 2025, 234-245.

29 V. Kumar, S. Matz, D. Hoogestraat, V. Bhavanasi, K. Parida, K. Al-Shamery and P. S. Lee, *Adv. Mater.,* 28, 2016, 6966–6975.

30 M. Iqbal, M. Faisal, H. Hassan, A. Afzal, S. Aftab, T. Zahid, and A. Rehman, *J. Energy Storage,* 52, 2022, 104847.

31 J. Gan, Y. Lim, N. Huang and H. Limb, *RSC Adv.,* 5, 2015, 75442–75450.

32 H. Rafique, M. Iqbal, S. Wabaidur, H. Hassan, A. Afzal, T. Abbas, M. Habila and E. Elahi, RSC Adv., 13, 2023, 12634-12645.

33 S. Nagamuthu and K. Ryu, *Sci. Rep.,* 9, 2019, 4864.

34 J. William, S. Balakrishnan, M. Murugesan, M. Gopalan, A. Britten and M. Mkandawire, *Mater. Adv*., 3, 2022, 8288–8297.

35 H. Hassan, M. Iqbal, N. Al-Shaalan, S. Alharthi, N. Alqarni, M. Amin and A. Afzal, *Nanoscale Adv*., 5, 2023, 4735-4751.

36 Q. Yang, F. Gong, Y. Wang, F. Yu and Y. Li, *ChemistrySelect*, 6, 2021, 9421-9426.

37 M. N. D. Cheruy, J.J. Aubert, J. C. Joubert, J. J. Capponi and H. Vincent, *Solid State Ion.*, 7, 1982, 171-176.

38 R. Guo, Y. Fan, and Y. Tang, *RSC Adv.*, 7, 2017*,* 23977–23981.

39 G. Botelho, J.C. Sczancoski, J. Andres, L. Gracia, and E. Longo, *J. Phys. Chem. C*, 119, 2015, 6293–6306.

40 P. C. Nagajyothi, T. Sreekanth, R. Ramaraghavulu, K. Devarayapalli, K. Yoo, S. Vattikuti and J. Shim, *J. Mater. Sci. Mater. Electron.* 30, 2019, 14890−14901.

41 D. Gupta, A. Kafle, S. Kaur, P. P. Mohanty, T. Das, S. Chakraborty, R. Ahuja and T. C. *J. Mater. Chem. A., 10, 2022,* 20616–20625.

View Article Online
DOI: 10.1039/D6NA00255B

42 S. T. Liu, J. S. Zhou and H. H. Song, *Small*, 14, 2018, 1703548.

43 X. Liu, W. Chen and H. Jiang, *Chem. Eng. J.,* 308, 2016, 889–896.

44 P.Y. Dong, Y.H. Wang, B.C. Cao, S.Y. Xin, L.N. Guo, J. Zhang and F.H. Li, *Appl. Catal. B: Environ.*, 45, 2013, 132–133.

45 L. Liu, Y. Qi, J. Lu, S. Lin, W. An, Y. Liang and W. Cui, *Appl. Catal. B: Environ.*, 183, 2016, 133-141.

46 R. Santos, T. Martins, G. Silva, M. Conceição, I. Nogueira, E. Longo and G. Botelho, *ACS Omega, 5,* 2020, 21651-21661.

47 D. Palles, I. Konidakis, C. P. E. Varsamis and E. I. Kamitsos, *RSC Adv.,* 6, 2016, 16697–16710.

48 S.W. Hu, L.W. Yang, Y. Tian, X.L. Wei, J.W. Ding, J.X. Zhong and P.K. Chu, *Appl. Catal. B: Environ.*, 163, 2015, 611–622.

49 R. Sari, M. Lubis, R. Sari, L. Kristak, A. Iswanto, E. Mardawati, W. Fatriasari, S. Lee, R. Reh, J. Sedliacik, M. Maulana, L. Suryanegara, B. Subiyanto and S. Maulana, *J. Compos. Sci.,* 7, 2023, 113.

50 C. Zheng, H. Yang and Y. Yang, *Mater. Trans., 58*, 2016, 298–301.

51 M. O. Kestner and A. L. Allred, *J. Am. Chem. Soc.*, 94, 1972, 7189.

52 L. Helseth, *J. Energy Storage,* 55, 2022, 105440.

53 C. Liu, Z. Yu, D. Neff, A. Zhamu and B. Jang, *Nano Lett*., 10, 2010, 4863-4868.

54 S. Nagamuthu and K. Ryu, *Sci Rep.*, 9, 2019, 4864.

55 J. William, I. Manohara Babu and G. Muralidharan, *Chem. Eng. J.*, 422, 2021, 130058.

56 K. Panigrahi, S. Mal, and S. Bhattacharyya, *J. Mater. Chem. A.,* 12, 2024,14334-14353.

57 S. S. Shalini, R. Balamurugan, S. Velmathi and A. C. Bose, *Energy & Fuels*, 36, 2022, 7104–7114.

58 M. Aghazadeh, A. N. Golikand and M. Ghaemi, *Int. J. Hydrog. Energy.*, 36, 2011, 8674–8679.

59 Q. Yang, F. Gong, Y. F. Wang, F. Yu and Y. Li, *ChemistrySelect*, *6*, 2021, 9421–9426.

60 G. C. Mohanty, D. R. Rout and A. Kumar, *J. Alloys Compd.,* 1053, 2026, 186265.

61 P. Matheswaran, P. Karuppiah and P. Thangavelu, *Ionics.,* 27, 2021, 1769-1780.

62 M. Z. Iqbal, S. R. Ali, M. M. Faisal, S. Siddique, S. Aftab and M. Alzaid, *Mater. Chem. Phys*., 291, 2022, 126638.

63 S. R. Ali, M. M. Faisal, S. L. Loredo, S. Gadi, and K. Sanal, *Ceram. Int.,* 4, 2023, 18311–18321.

64 F. S. Omar, A. Numan, S. Bashir, N. Duraisamy, R. Vikneswaran, Y. Loo, K. Ramesh and S. Ramesh, *Electrochim. Acta*, *273*, 2018, 216-228.

65 S. R. Ali, M. M. Faisal, S. Pushpan, N. P. Aguila, K.K. Singh, A. C. Pasarán, M. M. A. Rodríguez, E. M. Sánchez, A. T. Castro, S. L. Loredo, and K.C. Sanal, *Int. J. Energy Res.*, 46, 2022, 23757–23774.

66 H. Lindström, S. Södergren, A. Solbrand, H. Rensmo, J. Hjelm, A. Hagfeldt and S.-E. Lindquist, *J. Phys. Chem. B*, 101, 1997, 7717.

67 B. Yao, S. Chandrasekaran, H. Zhang, A. Ma, J. Kang, L. Zhang, X. Lu, F. Qian and C. Zhu, *Adv. Mater.,* 32, 2020, 1906652.

68 H. Hassan, M.W. Iqbal, N. H. Al-Shaalan, S. Alharthi, N. D. Alqarni, M. A. Amin and A. M. Afzal, *Nanoscale Adv.*, 5, 2023, 4735–4751.

69 G. Rutavi, D. J. Tarimo, V. M. Maphiri, V. N. Kitenge, and N. Manyala, *J. Alloys Compd***.**, 929, 2022, 167216.

70 M. Z. Iqbal, S. Siddique, M. Shahee, S. Alam and M. Alzaid, *Ceram. Int.,* 48, 2022, 15686–15694.

71 P. L. Taberna, P. Simon, and J. F. Fauvarque, *J. Electrochem. Soc.* 150, 2003, A292.

72 V. M. Maphiri, D. T. Bakhoum, S. Sarr, N. F. Sylla, G. Rutavi, and N. Manyala, *J. Energy Storage*, 52, 2022, 104967.

73 P. Kumari, S. K. Ghosh, C. Saha and K. Mallick, 2024). *J. Mater. Sci. Mater. Electron.*, 35, 2024, 1034.

74 A. C. Mendhe, A. Kore, S. D. Dhas, Y. Kim, R. Batool, A. Ghazal, and D. Kim, *Chem. Eng. J.*, 489, 2024, 151168.

75 F. S. Omar, A. Numan, S. Bashir, R. Vikneswaran, K. Ramesh and S. Ramesh, *J. Energy Storage*, 32, 2020, 101850.

76 H.L. Fernandez-Canque, Analog electronic applications fundamentals of design and analysis, CRC press, 2019.

77 C. May, Passive Circuit Analysis with LTspice: An Interactive Approach, Springer Nature, 2020.

78 A.S. Sedra and K.C. Smith, Microelectronic Circuits, Oxford University Press, 2014.

79 P. Horowitz and W. Hill, W. *The art of electronics*. Third Edition, 2015, Cambridge University Press, New York.

80 E. Rodriguez-Villegas, A. Casson and P. Corbishley, IEEE transactions on circuits and systems, 2011, 58, 351-355

View Article Online
DOI: 10.1039/D6NA00255B

Figure caption:

Figure 1: (A) XRD pattern of silver phosphate within the range from 20-90° and unit cell representation of cubic silver phosphate. (B) XPS survey spectrum of hexamine-silver phosphate composite and high-resolution Ag 3d spectrum (inset). High resolution deconvoluted spectra for (C) P 2p, (D) O 1s, (E) C 1s and (F) N 1s.

Figure 2: (A and B) Dark-field transmission electron microscopy images of hexamine stabilized silver phosphate particles with different magnifications. (C) Transmission electron microscopy image of a single silver phosphate particle.

Figure 3: (A) Field emission SEM image of the hexamine stabilized silver phosphate composite. (B) Energy dispersive X-ray spectrum (EDS) of silver phosphate. (C-G) Individual EDS elemental mapping of Ag, P, O, C and N, respectively.

Figure 4: (A) Raman and (B) FTIR spectra of hexamine-stabilized silver phosphate composite system.

Figure 5: (A) Cyclic voltammogram of SPO-modified electrode under the scan rates ranging from 4 to 50 mV.s^{-1}. Inset: CV profile at 8 mV.s^{-1}. (B) GCD profile of SPO-modified electrode under the current densities ranging from 1.0 to 3.4 A.g^{-1} (main panel) and 4.0 to 5.8 A.g^{-1} (inset). (C) Specific capacity vs current density for SPO-modified electrode. (D) Upper panel: The electrode retained 91 % of capacity and maintaining a Coulombic efficiency of 99 %, at a current density of 2.2 A.g^{-1}, based on 2000 charge-discharge cycles. Lower panel: first- and last-five GCD cycles.

Figure 6: (A) Cyclic voltammogram of SPO||AC-based asymmetric device within scan rate of 4-50 mV.s^{-1}. Figure 7: Galvanostatic charge-discharge profile of the asymmetric device under the various current densities ranging from 0.5 to 1.7 A.g^{-1}. Figure 8: Capacity retention and coulombic efficiency of the asymmetric device for 5000 cycles at 0.9 Ag^{-1}; inset: first and last five cycles of the device. Figure 9: Energy density and power density as a function of current density of the asymmetric device.

Figure 7: (A) Peak current (I_p) as a function of scan rate (ϑ), in log scale, of the asymmetric device. (B) Bar diagram for the capacitive and diffusive contributions of the device under various scan rate ranging from 4 to 50 mV.s^{-1}. (C) Bode plot, phase angle as a function of frequency, of the device. (D) Graphical representation for the real (C') and imaginary (C'') capacitance as a function of frequency.

Figure 8: (A) Cyclic Voltammogram of SPO-based symmetric devices within the scan rates ranging from 10-70 mV.s^{-1}. (B) Galvanostatic charge-discharge profile of the device under the various current densities ranging from 0.6 to 2.4 A.g^{-1}. (C) Capacity retention and coulombic efficiency of the device for 5000 GCD-cycles, Inset: first and last five GCD-cycles at the current density of 1.2 A.g^{1}. (D) Energy density and Power density as a function of current density of the device.

View Article Online
DOI: 10.1039/D6NA00255B

Figure 9: (A) Peak current (I_p) as a function of scan rate (ϑ), in log scale, for the symmetric device. (B) Bar diagram for the capacitive and diffusive contributions of the device under various scan rate ranging from 10 to 70 mV.s^{-1}. (C) Bode plot, phase angle as a function of frequency, of the symmetric device. (D) Graphical representation for the real (C') and imaginary (C'') capacitance as a function of frequency.

Figure 10: Low pass filter circuit and experimental setup. (A and B) First-order LPF configurations, asymmetric (R_1 = 50 kΩ and C_1 = 3.4 mF) and symmetric (R_2 = 500 kΩ, C_2 = 0.45 mF). (C and D) Second-order LPF with two cascaded RC stages (R_1 = 50 kΩ, C_1 = 3.4 mF and R_2 = 500 kΩ, C_2 = 0.45 mF).

Figure 11: Voltage vs Time outputs (A) First order LPF: C_1 = 3.4 mF, f_c = 0.93 mHz (B) First order LPF: C_2 = 0.45 mF, f_c = 0.7 mHz (C) Second Order LPF: C_1 = 3.4 mF, C_2 = 0.45 mF, f_c = 0.51 mHz.

Figure 12: Bode plots representing the frequency-dependent behavior of asymmetric, symmetric and cascaded second-order RC low-pass filters. (A) magnitude response and (B) phase response.

View Article Online
DOI: 10.1039/D6NA00255B

Figure: 1

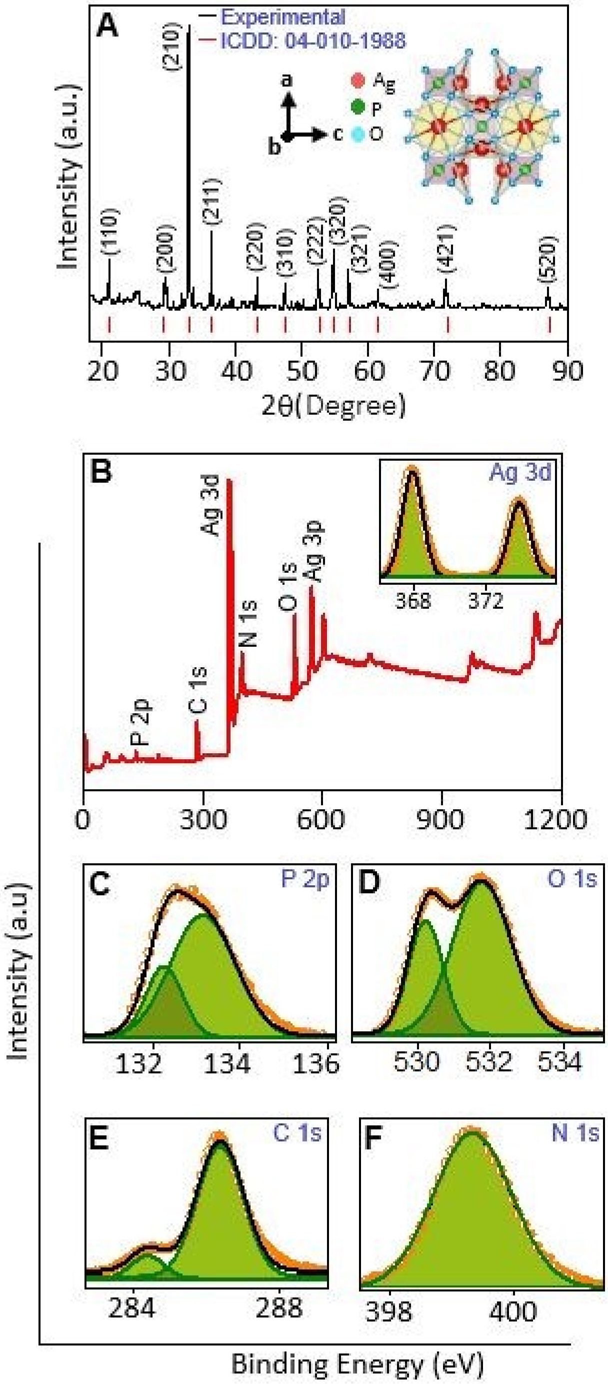

View Article Online
DOI: 10.1039/D6NA00255B

Figure: 2

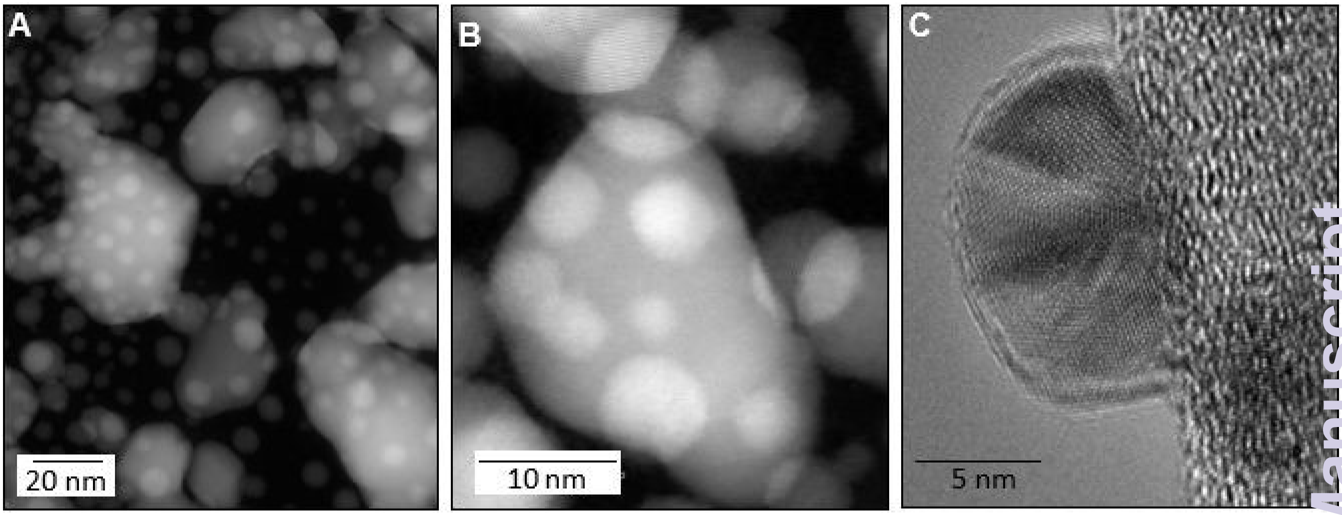

View Article Online
DOI: 10.1039/D6NA00255B

Figure: 3

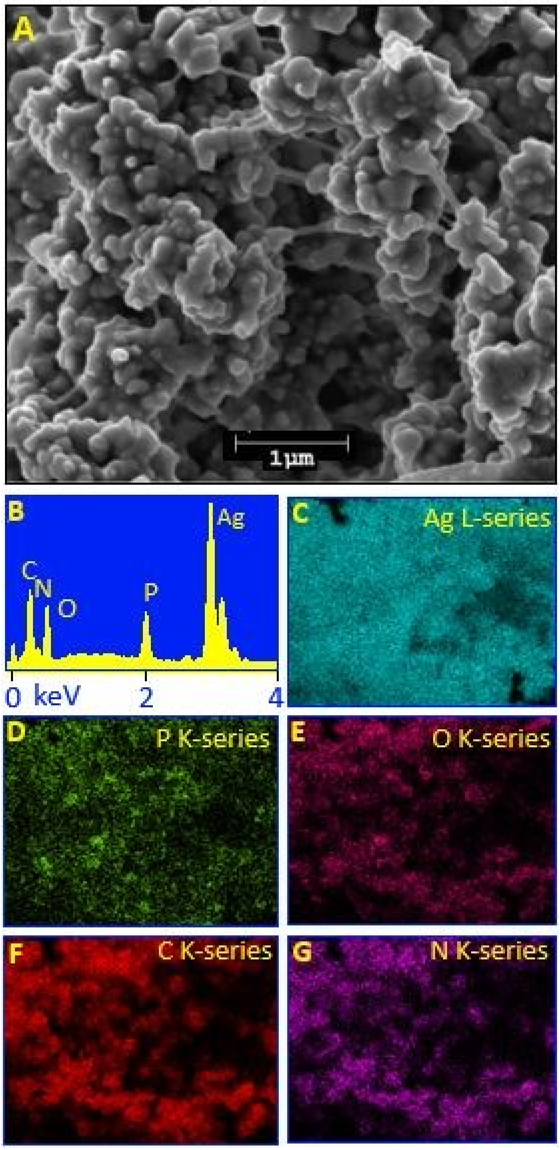

View Article Online
DOI: 10.1039/D6NA00255B

Figure: 4

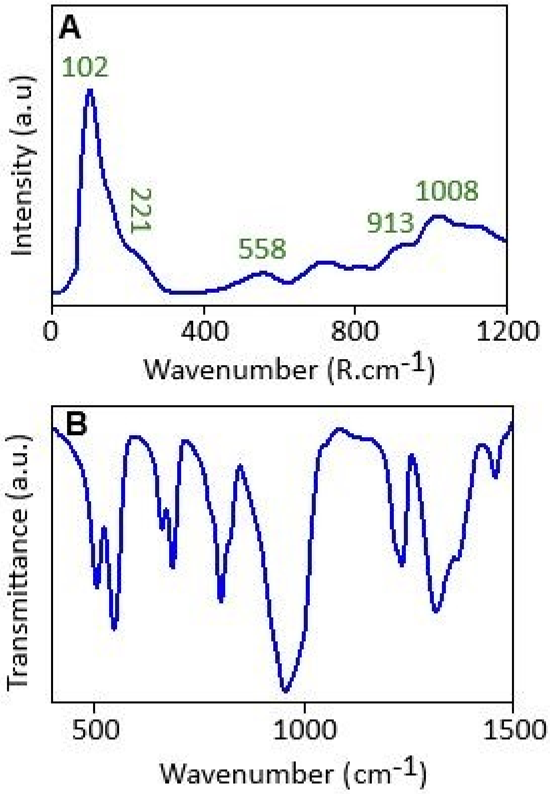

View Article Online
DOI: 10.1039/D6NA00255B

Figure: 5

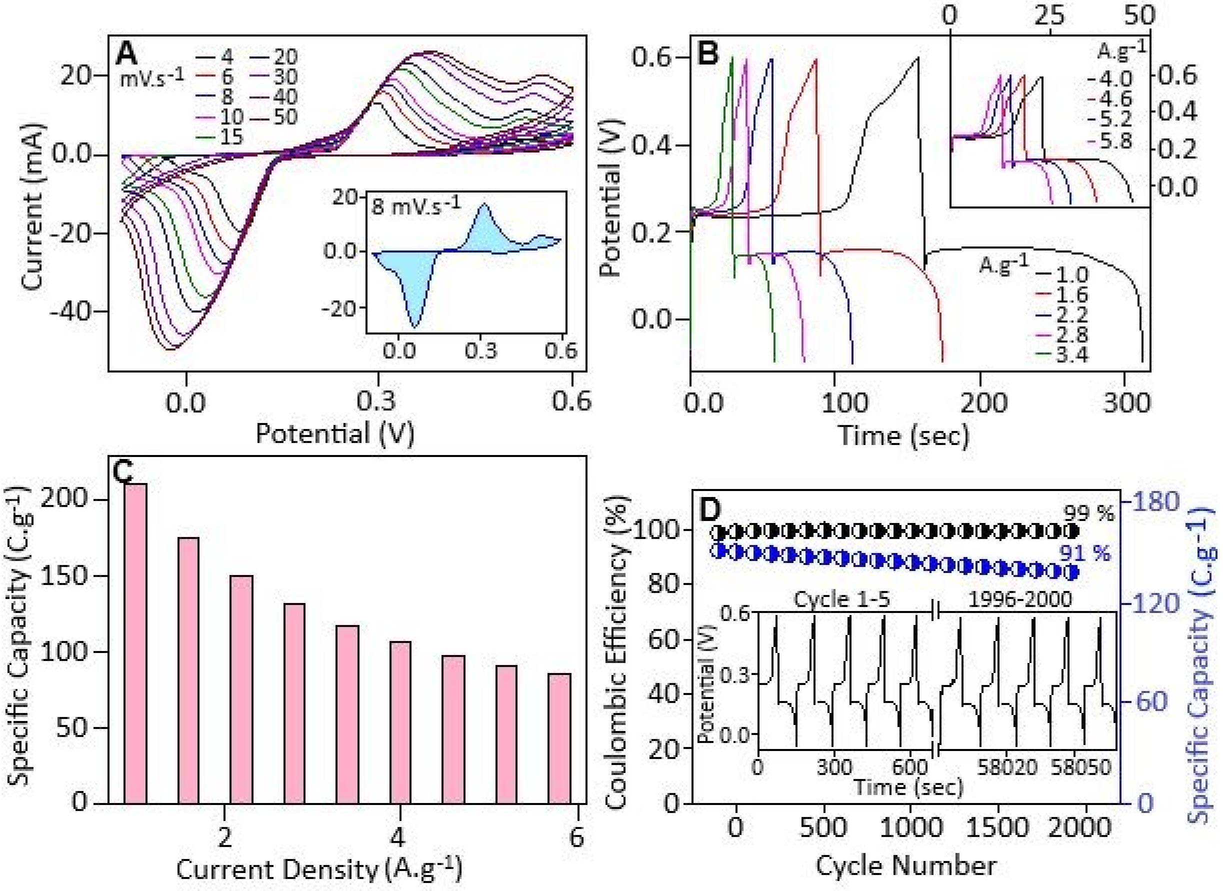

View Article Online
DOI: 10.1039/D6NA00255B

Figure: 6

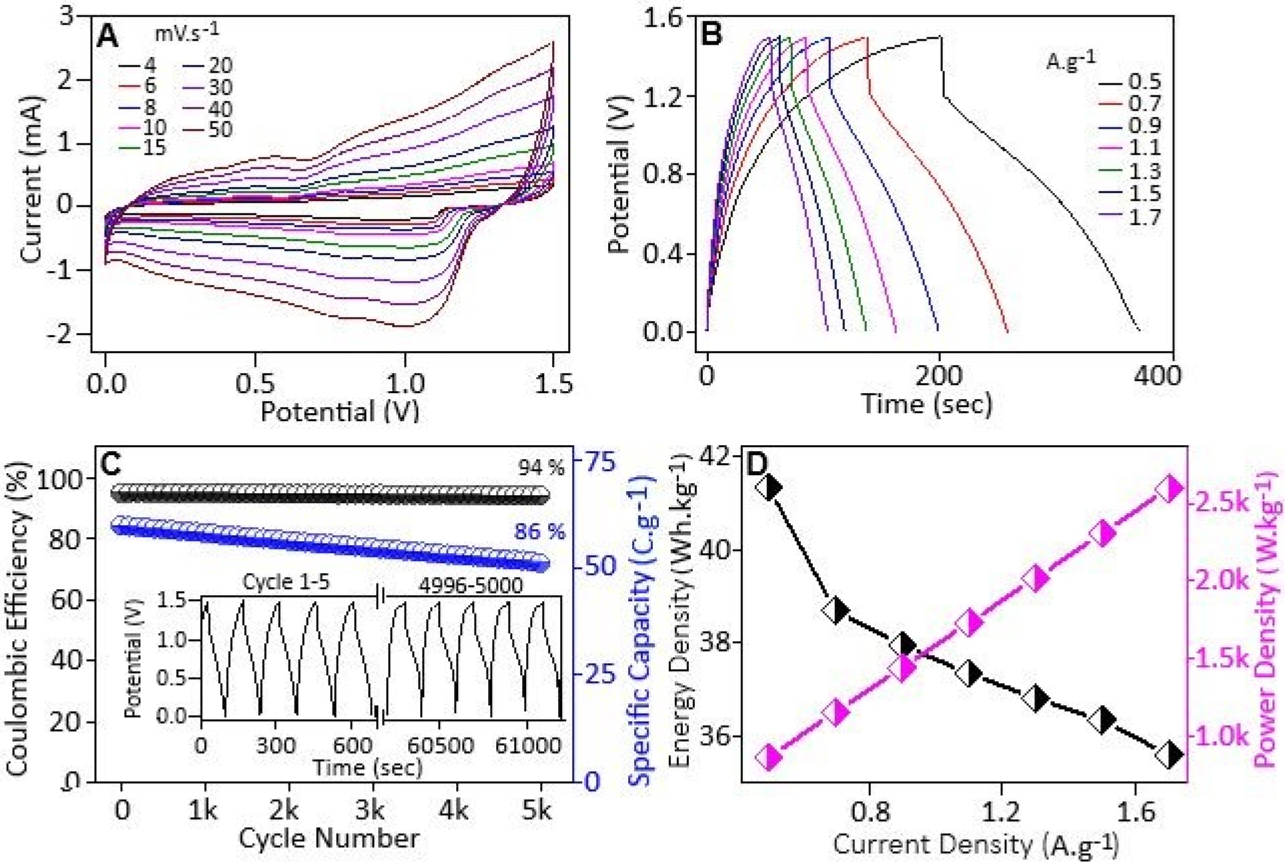

View Article Online
DOI: 10.1039/D6NA00255B

Figure: 7

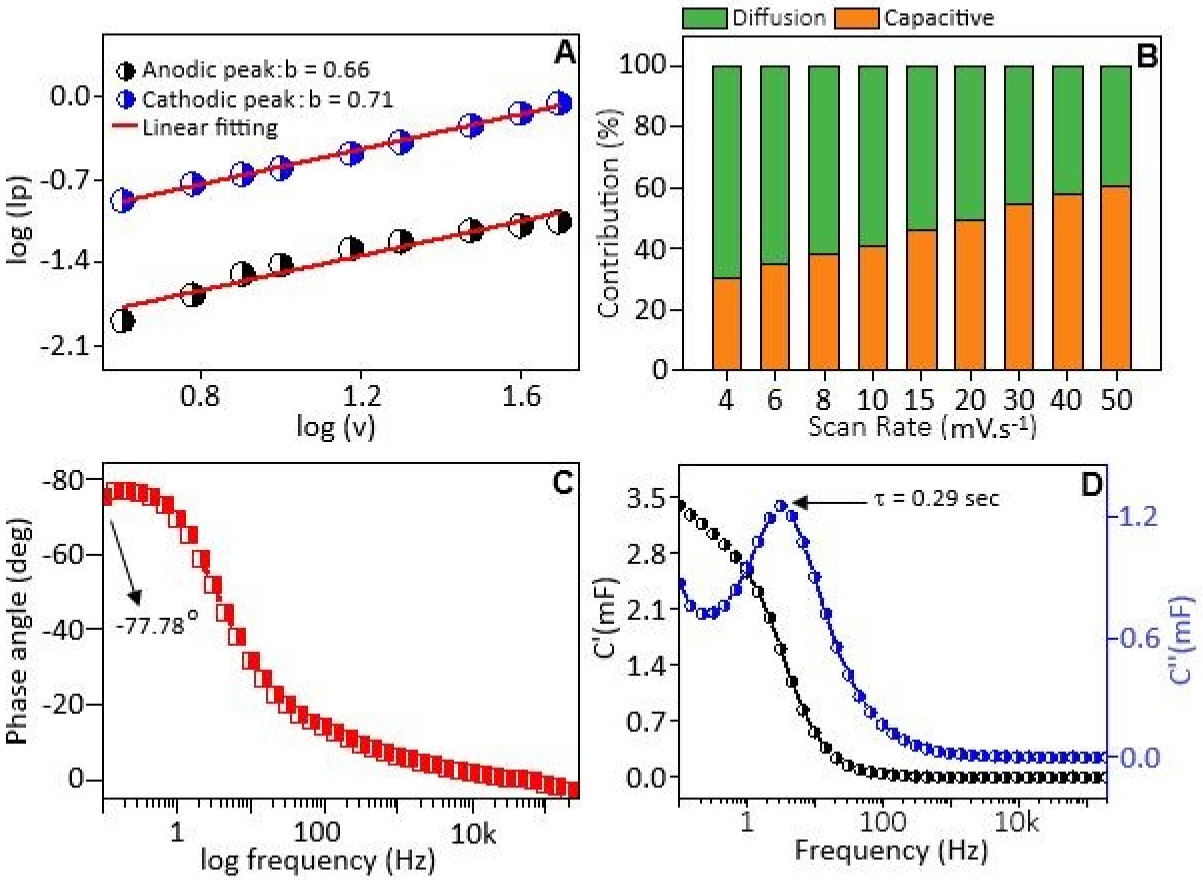

View Article Online
DOI: 10.1039/D6NA00255B

Figure: 8

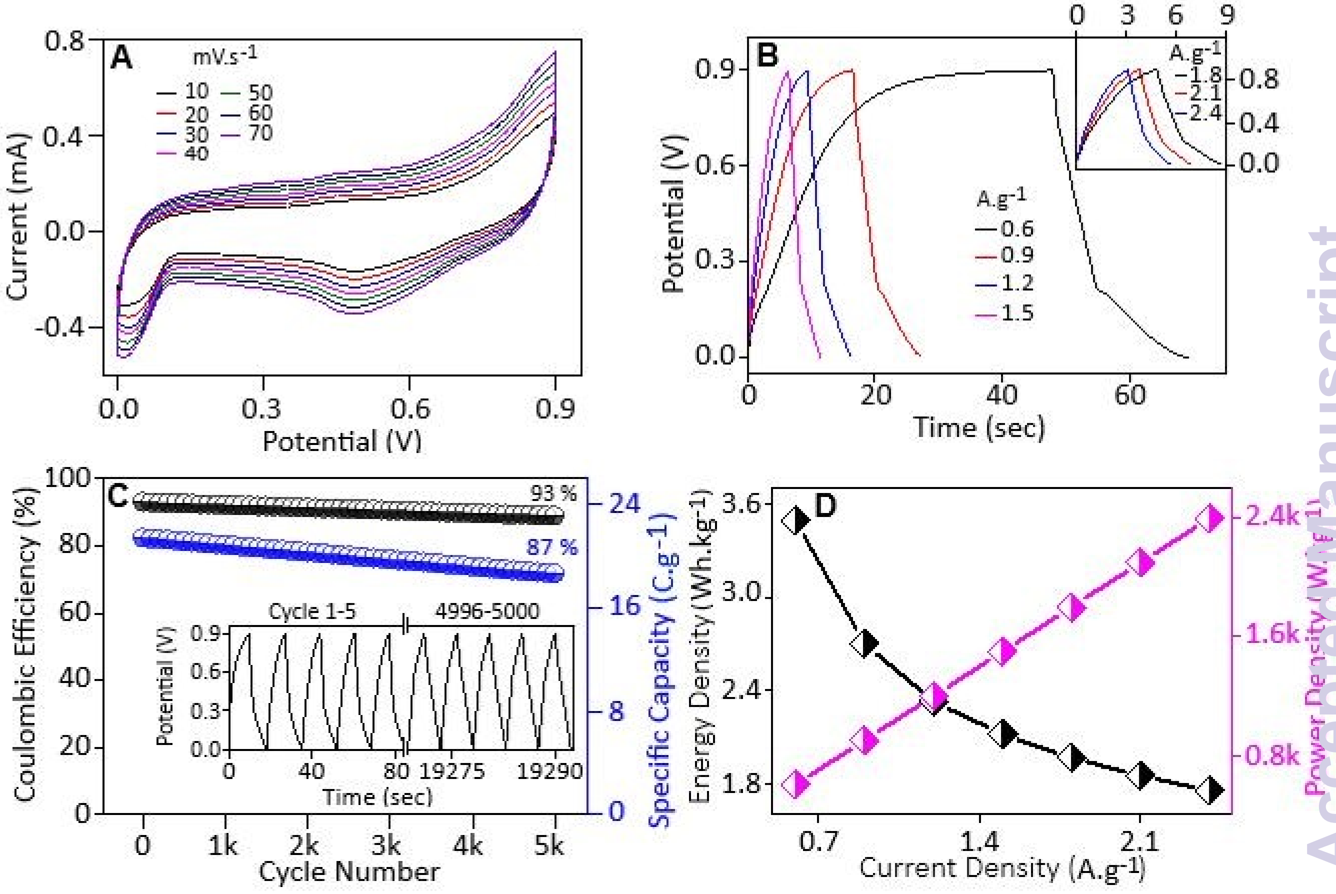

View Article Online
DOI: 10.1039/D6NA00255B

Figure: 9

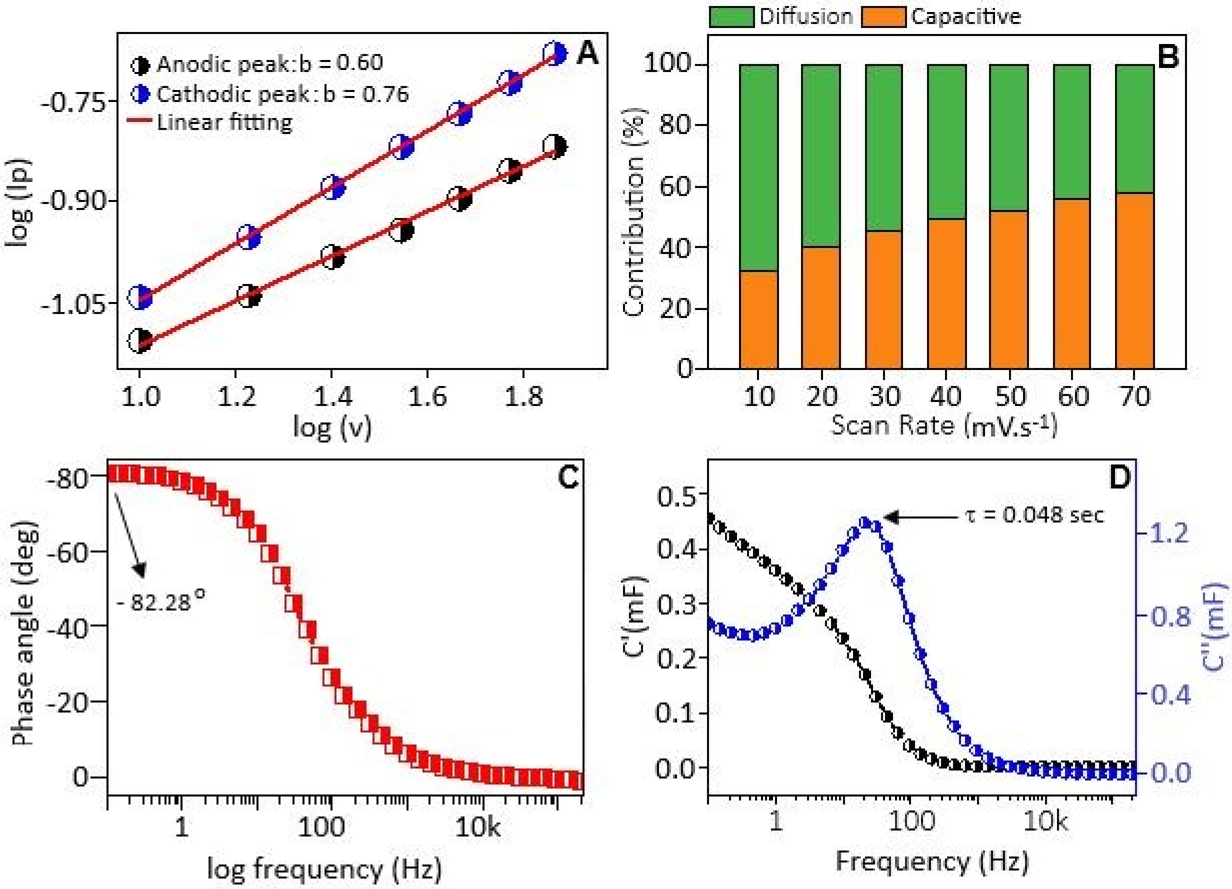

View Article Online
DOI: 10.1039/D6NA00255B

Figure: 10

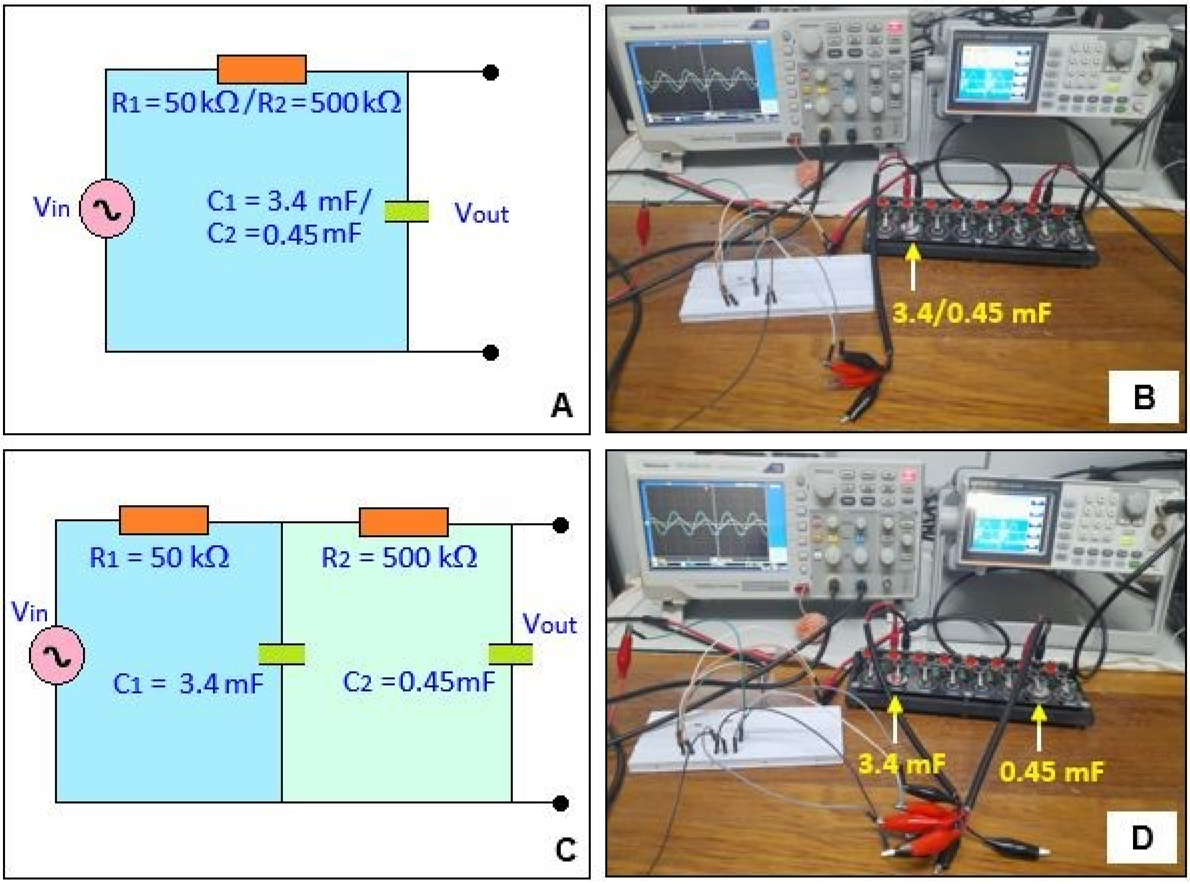

View Article Online
DOI: 10.1039/D6NA00255B

Figure: 11

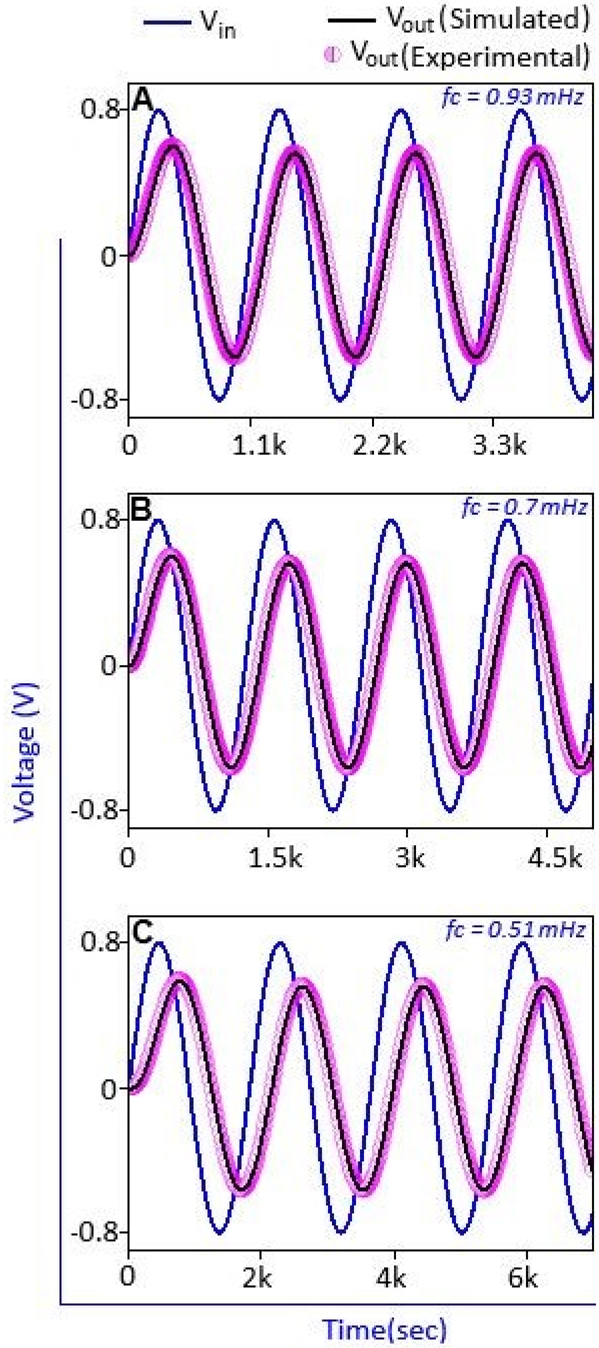

View Article Online
DOI: 10.1039/D6NA00255B

Figure: 12

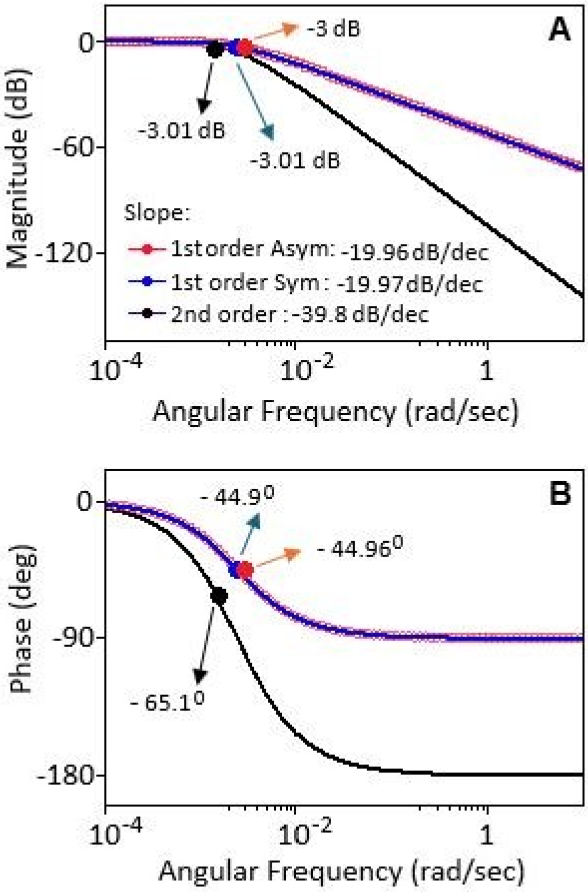

View Article Online
DOI: 10.1039/D6NA00255B

Data Availability Statement

The data supporting the findings of this study will be made available upon reasonable request.